Extending mARC II Arc-Jet Test Duration via Design and Implementation of Model System Cooling Sleeve

Kathleen M. Edwards*
Sierra Lobo Inc. at NASA Ames Research Center, Moffett Field, California, 94035, USA

Jocelino Rodrigues†
NASA Postdoctoral Program at NASA Ames Research Center via ORAU, Moffett Field, California, 94035, USA

Daniel Philippidis‡
NASA Ames Research Center, Moffett Field, California, 94035, USA

The mARC II is a 30 kW arc-jet facility at NASA Ames Research Center used to generate high-enthalpy flows for low-cost thermal protection system (TPS) technology development. Sustained operation of downstream instrumentation and material samples is constrained by thermal loading transmitted through the arc-jet test environment, limiting achievable run times and experimental throughput. This work presents the design, integration, and validation of a cooling sleeve implemented on the sweep arm drive motor feedthrough to mitigate thermal accumulation during testing. The addition of the cooling sleeve is a simple, robust upgrade that translates directly into enhanced facility capability by supporting longer run durations, reduced turnaround time, and higher throughput.

I. Introduction

Arc-jet testing remains a cornerstone for material and TPS research where controlled, high-enthalpy environments are required [1]. The mARC II facility supports this mission with a low-cost, flexible platform tailored to the development of diagnostic techniques, instrumentation approaches, and material evaluation methods within a laboratory-scale setting [2–11]. Prior work documented new measurement capabilities and started to map the operating envelope of the two-disk arc-heater configuration in air, establishing reliable ranges for stagnation heat flux, stagnation pressure, and enthalpy [12–14]. In parallel with these characterization efforts, we target a persistent bottleneck that limits experimental cadence and throughput: thermal constraints on the motor feedthrough. This paper details the corresponding cooling solution and its measured impact on facility operations.

II. Experimental setup

The mARC II is a 30 kW segmented constricted arc-heater that uses a Hypertherm MAX200 plasma cutter for power supply and gas flow management. The cathode is housed inside the Hypertherm torch body and integrated into the actively water-cooled arc-heater. The heater was designed in-house; inspired by the larger arc-jet facilities at the Ames Arc-Jet Complex [15, 16]. It is composed of the cathode, constrictor disks, an anode, and a convergent-divergent nozzle [17, 18]. Once a stable arc is produced inside the column, a plasma jet is exhausted into the test box. The mARC II test box can reach medium (fine) vacuum conditions before the start of each run and to maintain constant pressure after the addition of the test gas and arc-on. The nozzle flow is underexpanded which is desirable for testing of samples [19]. The current version of the mARC II sweep arm system consists of a driving rotary motor, a vacuum Ferrofluidic® feedthrough from Ferrotech, a shaft, and a sweep arm. In this work, we aim to improve mARC II testing capabilities through the addition of a cooling sleeve for the feedthrough.

*Mechanical Engineer, Thermophysics Facilities Branch, Entry Systems & Technology Division. (✉ kathleen.m.edwards@nasa.gov).
†NPP Research Fellow, Thermophysics Facilities Branch, Entry Systems & Technology Division. AIAA Young Professional. (✉ jocelino.rodrigues@nasa.gov).
‡Facility Engineer, Thermophysics Facilities Branch, Entry Systems & Technology Division.

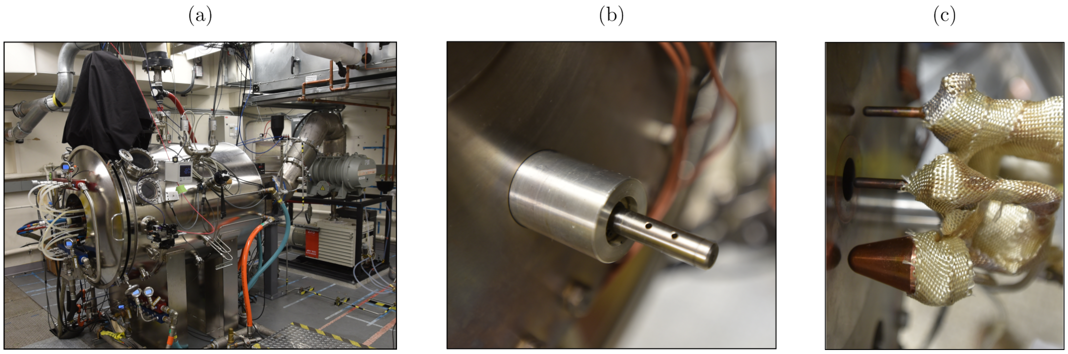

Fig. 1 Experimental setup: (a) miniature Arc-jet Research Chamber (mARC II); (b) uncooled vacuum feedthrough system and motor shaft; (b) trident sweep arm with high-temperature Refrasil insulating material wrapping.

III. Feedthrough cooling sleeve

A. Design problem and objectives

Currently, the mARC II sweep arm is directly attached to the shaft of a rotary motor that uses a Ferrofluidic® vacuum feedthrough. This device allows the motor shaft to pass through a vacuum boundary. With increased interest in novel TPS development, it is expected that customers will request long sample dwell times (>3 mins per sample). Preliminary experimental data shows that the sweep arm temperature increases quickly, despite the use of high-temperature Refrasil insulating material. According to the manufacturer, the entire feedthrough has a maximum operating temperature of 80 °C. At the target dwell times for sample screening, and without active cooling, the plasma flow's heat will transfer from the arm, to the shaft, and then to the ferrofluid inside the seal quickly, reaching the limit temperature before a full set of three samples on the trident can be screened.

The proposed solution is an aluminum sleeve that allows cooling water to directly contact the exterior of the feedthrough in order to cool the inner ferrofluid.

B. Analyses

We use a three-stage analysis strategy which combines fluid dynamics simulations, heat transfer modeling, and a thermo-mechanical stress analysis.

1. Fluid dynamic simulation

The first step is running a fluid dynamic simulation to understand what pressure will be present at the cooling sleeve based on the supply pressure and geometric constraints in between. In order to do this, we use AFT Fathom, a 1D incompressible flow solver commonly used to calculate pressure drop and pipe flow distribution in piping systems [20, 21].

1.1. Setup

The Fathom analysis uses the supply and return pressures as boundary conditions. The sleeves themselves are modeled as valves with a set C_v:

$$C_v = K\dot{V}\sqrt{\frac{SG_{\mathrm{w}}}{\Delta p}}\ , \tag{1}$$

where $\dot{V} = \dot{m}/\rho = \dot{m}/1000 = 3.185 \times 10^{-4}$ m^3/s is the volumetric flow rate for water, p is the static pressure in kPa, and $SG_{\mathrm{w}} = 1$ is the specific gravity for water, and $K = 4.16 \times 10^4$ is an SI unit conversion factor. The piping cross-section, material, and number of bends were used as inputs to create the piping network model.

1.2. Results

Checking the results shows that the pressure drop across each sleeve is the same and matches the corresponding pipes

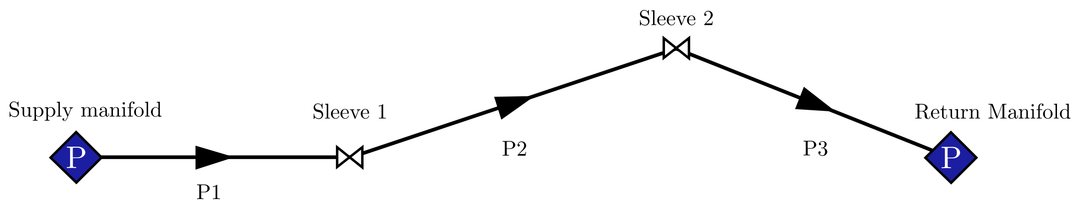

Fig. 2 Piping system in Fathom.

inlet/outlet pressures as expected. Additionally, if we plug the pressure drop across the sleeves and the volume flow rate back into Eq. (1), we obtain a C_v that is only a 0.16% difference from the original value with arbitrary pressures and volume flow rate. With these sanity checks, the primary result we are concerned with is the inlet/outlet pressures for the two sleeves to use as boundary conditions in the heat transfer modeling presented in §III.B.2. Additionally, we confirm that our pumps will be able to handle the estimated volume flow rate.

2. Heat transfer modeling

This section presents heat-transfer simulations performed in ANSYS Fluent 2025 R2, with pressure boundary conditions prescribed from the Fathom one-dimensional solver results described in the previous section. The purpose of these heat transfer simulations is to determine if a cooling sleeve applied to the outside of the motor feedthrough will keep the assembly under the maximum operating temperature at maximum heating at steady state.

2.1. Material properties

The default material properties in Ansys Fluent are used for the aluminum sleeve and ferrofluid cover, and cooling water – shown in Table 1. Data for 440C Stainless Steel is from the Aerospace Structural Metals Handbook [22]. For the ferrofluid, the material properties were initially taken for a similar ferrofluid from the same manufacturer; however, the exact properties are proprietary [23, 24]. In order to test the sensitivity of the ferrofluid thermal conductivity, another analysis was run with a lower value of 0.13 W/(m-K) which is similar to other synthetic ester oils [25]. This resulted in a less than 0.15% increase in the ferrofluid temperature; however, the lower value was still used to produce more conservative results. Another simplification in the analysis is that the ferrofluid is modeled as a solid, since we are not concerned with the movement of the liquid, and any mixing would result in more uniform cooling and an overall lower maximum temperature.

2.2. Numerical setup

The inlet configuration corresponds to a jet interacting with a confined crossflow, a canonical class of flows characterized by strong shear-layer development and mixing-driven transport [26, 27]. Curvature-induced secondary motions characteristic of flow in curved ducts are well documented in canonical analyses of turbulent internal flows [28].

Simulations were performed using ANSYS Fluent (2025 R2) employing the pressure-based solver formulation. A steady-state solution strategy was adopted with absolute velocity formulation. Turbulence closure was provided by the two-equation shear stress transport (SST) k–ω model, selected for its robust performance in internal flows involving adverse pressure gradients, curvature, and possible separation [29–34]. Low Reynolds number corrections were not activated. Near-wall treatment utilized Fluent's correlation-based automatic wall formulation. Default model constants were retained, with the production limiter enabled to enhance numerical stability. Curvature correction, corner flow correction, and viscous work terms were not included.

The energy equation was enabled in all cases to resolve thermal transport effects. Turbulent heat flux modeling employed a constant turbulent Prandtl number, with both the energy and wall Prandtl numbers specified as $Pr_t = 0.85$, consistent with widely adopted engineering practice for internal turbulent flows [35]. Pressure–velocity coupling was handled using the coupled solution scheme, with fluxes evaluated via the Rhie–Chow momentum-based interpolation [36]. Spatial discretization employed a finite-volume formulation and spatial gradients were computed using the least-squares cell-based method, consistent with standard CFD practice [37]. Second-order discretization was applied consistently across governing equations: pressure employed a second-order scheme, while momentum, turbulent kinetic energy, specific dissipation rate, and energy equations utilized second-order upwind formulations. To enhance convergence robustness, a pseudo-transient continuation approach was employed using a global time-step method, a

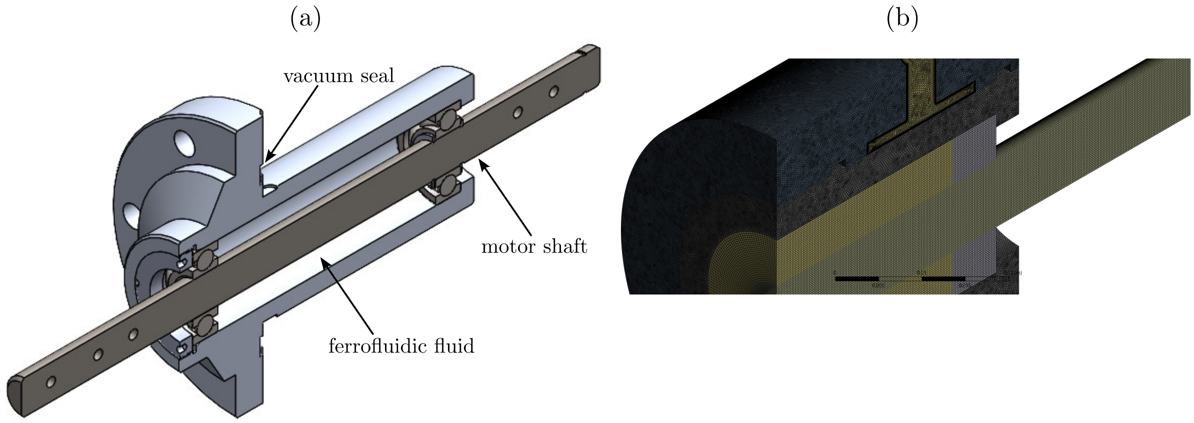

Fig. 3 Vacuum feedthrough geometry and numerical discretization: (a) original CAD assembly; and (b) full three-dimensional mesh showing refinement in regions of interest.

strategy commonly adopted to accelerate steady-state convergence in nonlinear flow systems [38, 39]. The fluid time scale was determined automatically with a conservative length-scale formulation and a time-scale factor of unity.

Solution stabilization was controlled through explicit relaxation factors, consistent with standard iterative solution practices for segregated and coupled finite-volume solvers [40]. Pressure and momentum relaxation factors were set to 0.5, while relaxation factors for turbulent kinetic energy, specific dissipation rate, and energy were set to 0.75. The turbulent viscosity relaxation factor was kept at unity.

Table 1 Material properties for heat transfer model.

Material	λ [W/m-K]	ρ [kg/m^3]	μ [kg/m-s]
6061 T6 Aluminum	202.4	2719	–
440C Stainless Steel	24.2	7800	–
Ferrofluid	0.13	1240	–
Water	0.6	998.2	0.001003

2.3. Mesh

The steel shaft and bearing, ferrofluid, aluminum cover, cooling water, and aluminum sleeve are all modeled in Fluent. The bearing in the Ferrofluidic® feedthrough is modeled as a solid piece of 440C stainless steel for simplicity. Boundary layer inflation on the fluid domain was defined using a prescribed first-layer thickness. The final domain and mesh is shown in Fig. 3, and mesh statistics are in Table 2.

For the SST k–ω model, the wall-adjacent spacing was selected to resolve the near-wall region, yielding an area-weighted mean $y^+ = 1.36$ across wetted surfaces. Local maxima are confined to the inlet-duct entrance region, where the imposed inlet condition transitions to a developing internal boundary layer, producing locally elevated wall shear and thus slightly larger y^+. The maximum observed value is $y^+ = 7$, and the y^+ histogram confirms that values above $y^+ = 5$ occur over a negligible fraction of the wall area. All wall-adjacent cells satisfy $y^+ < 10$, consistent with near-wall-resolved RANS without wall-function dependence.

Table 2 Mesh statistics for heat transfer modeling.

Total Nodes	Total Elements	Element Size	Max Skewness	Average Skewness
3,935,372	17,718,911	0.254 mm	0.897	0.193

2.4. Boundary conditions

The boundary conditions for the cooling water are taken from the Fathom results while the heating input is taken from limited mARC II data. Symmetry boundary conditions are applied to the right and front plane of the model and exterior faces that don't have applied heating are assumed to be adiabatic. The most downstream sleeve is modeled since it will have the highest fluid temperatures. The inlet pressure is taken from the Fathom results.

The primary source of heating for the sleeve and ferrofluid is conduction through the stainless steel swing arm. During current testing, a self-imposed temperature limit of approximately 100 °C was assumed for the motor shaft, reflecting a conservative engineering design margin which accounts for safety factors to guarantee it operates reliably without failure. To learn about the heat transfer behavior during a run, the sweep arm is instrumented with a surface thermocouple (Omega SA1-K) to measure the increase in temperature of the sweep arm during the dwell (Fig. 4) for a run at 4 kW with the sweep arm at 69 mm from the nozzle. The data was collected before, during, and after insertion in the flow. The data from this run is used for the initial heat calculation. Since this run was done using 4 kW of arc power, the heat is scaled to represent the maximum heating scenario with 30 kW of power.

The heating is then calculated using:

$$Q_1 = mc_p\Delta T \ , \tag{2}$$

where m = 0.0913 kg for the sweep arm and c_p = 502.4 J/kg-K for stainless steel. We assume the ΔT is computed between the linear temperature increase regime (100 s and 450 s):

$$\Delta T = 75\ ^\circ\mathrm{C} - 30\ ^\circ\mathrm{C} = 45\ ^\circ\mathrm{C} = 45\ \mathrm{K}\ . \tag{3}$$

As such, the heat energy (2) can be computed:

$$Q_1 = (0.0913\ \mathrm{kg}) \times (502.4\ \mathrm{J/kg\text{-}K}) \times 45\ \mathrm{K} \ = \ 2057.3\ \mathrm{J}\ . \tag{4}$$

The heat power can be calculated by using the duration:

$$\dot{Q}_1 = \frac{2057.3\ \mathrm{J}}{350\ \mathrm{s}} \ = \ 5.88\ \mathrm{W}\ . \tag{5}$$

Because this test case was conducted at a 4 kW operating condition, the corresponding heat load was linearly extrapolated to the maximum power-supply condition of 30 kW. This scaling is treated as a conservative engineering estimate for the maximum-load case:

$$\dot{Q}_{\max} = (5.88\ \mathrm{W}) \left(\frac{30\ \mathrm{kW}}{4\ \mathrm{kW}}\right) \ = \ 44.10\ \mathrm{W}\ . \tag{6}$$

The resulting thermal load is transferred to the shaft through contact with the swing-arm mount. Contact resistance at this interface is neglected, both for simplicity and to provide a conservative estimate of the heat conducted into the

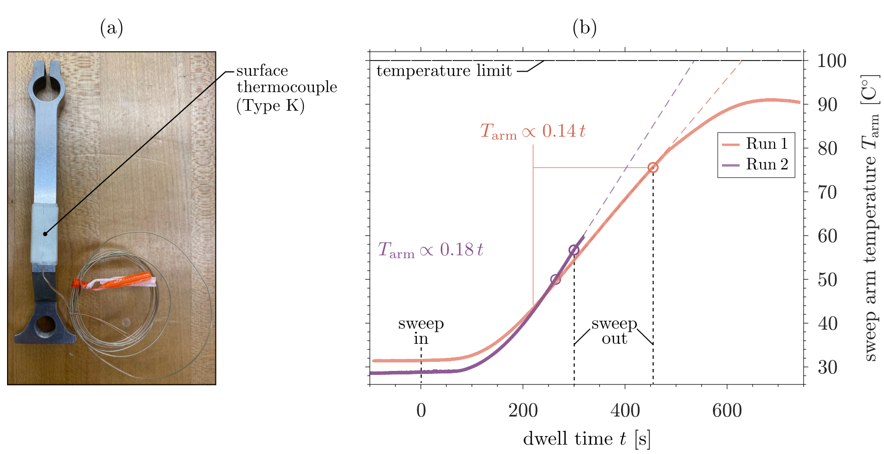

Fig. 4 Heat transfer scaling: (a) single-mount sweep arm instrumented with a surface Type K thermocouple; (b) measured sweep-arm temperature as a function of dwell time for Run 1 (4.0 kW) and Run 2 (4.4 kW).

shaft. The contact area is approximately 9.77×10^{-4} m^2, such that the heat flux is:

$$\dot{q} = \frac{44.10 \text{ W}}{(9.77 \times 10^{-4}) \text{ m}^2} = 45,138 \text{ W/m}^2 . \tag{7}$$

This is the heating value applied to the shaft in Fluent. To calculate the inlet temperature, we assume that all of the heat applied to the shaft upstream is absorbed by the upstream cooling water, and that the maximum temperature limit of the cooling system is 32.2 °C. The mass flow rate is taken from the Fathom results.

2.5. Results

The cooling sleeve to be fabricated has a maximum temperature near an O-ring, seen in Figure 5(a), but is only 311 K (40 °C) and well within operating temperature range of many O-ring materials. The maximum temperature of the inner ferrofluid is 341 K (68 °C), seen in Figure 5(a) where it contacts the shaft. This maximum temperature is expected to be further dissipated by both free-flow convection and forced convection during shaft movement and is still below its maximum operating temperature of 353 K (80 °C).

The bearing has a max temperature of 392 K (119 °C) furthest from the ferrofluid and closest to the shaft, seen in Figure 5(a). This is the above operating temperature of the feedthrough system, though the overall volume above 353 K (80 °C) is relatively low. The operating temperature of the bearing would be dictated by the dropping point of the grease. While the specific grease properties were not available from the manufacturer, most lubricating greases have dropping points exceeding 392 K (119 °C), indicating that the bearing is likely operating within its allowable temperature range. A thermocouple will be installed on the shaft between the model holder and the bearing to monitor this temperature.

The end of the shaft reaches a much higher temperature than the rest of the bodies at 1134 K (861 °C), as can be verified in shown in Fig. 5(b). This is expected since it's the furthest from the cooling water, is directly contacting the source of heating, and the steel has poor conductivity. However, 440C Stainless Steel has a rather high yield stress and melting temperature at 1755 K (1482 °C) so it is expected to withstand the small stresses applied. The cooling water only heats about 1 K between the inlet and outlet of the sleeve. This shows that we have a large enough flow rate to ensure the entire sleeve is receiving appropriate cooling.

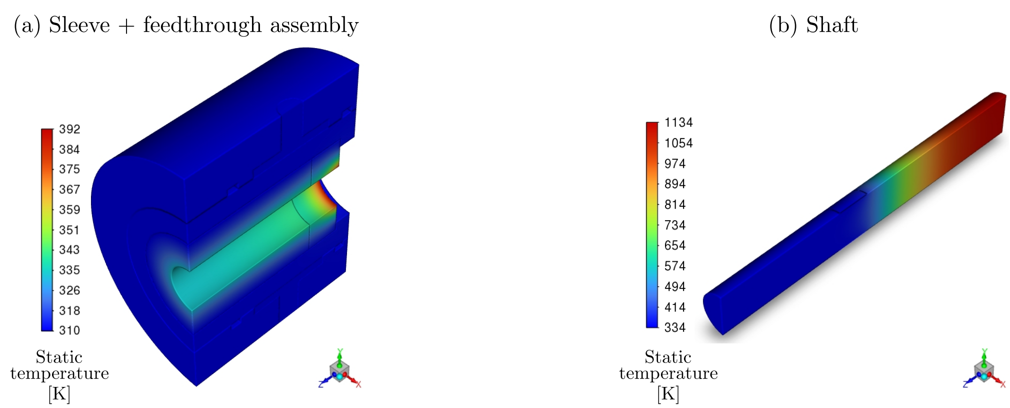

Fig. 5 Computed static temperature distributions: (a) sleeve and feedthrough assembly; and (b) motor shaft.

3. Thermo-mechanical stress analysis

In order to predict how the cooling sleeve deforms and what stresses develop when limit load temperatures and pressures are applied, we employ ANSYS Mechanical Analysis to complete a thermo-mechanical stress analysis.

3.1. Material properties

The material used for the sleeve is round tube aluminum alloy ASME SB-241 A96061 T651 and all properties are taken from the ASME BPVC Section II-D 2023 [41]. Baseline values are listed here, but the elastic modulus was input as a tabulated function of temperature up to 260 °C.

3.2. Mesh

A quarter symmetry was used to simplify the analysis, as shown in Fig. 6. Tetrahedral elements were used to mesh the cooling sleeve and an element size of 0.3 mm was used based on a mesh sensitivity study. Mesh statistics are detailed in Table 3.

Table 3 Mesh statistics for thermo-mechanical stress analysis.

Total Nodes	Total Elements	Element Size	Max Aspect Ratio	Average Aspect Ratio	Elements with Aspect Ratio >3
3,926,826	2,870,353	0.3 mm	6.715	1.7662	1.42%

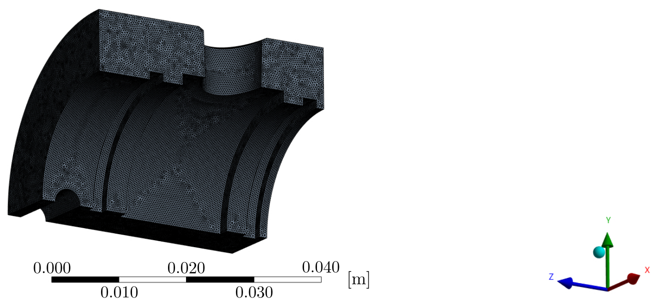

Fig. 6 Three-dimensional mesh of cooling sleeve with quarter symmetry.

3.3. Boundary conditions

A frictionless support boundary condition was applied to both symmetry faces. Since a set screw will be used to attach the sleeve to the outside of the feedthrough, a fixed support boundary condition was used where the treads will be.

In this analysis the maximum design pressure for the system is applied and the stress compared to the ASME allowable stress at design temperature for a worst case approximation.

The design pressure was based on the maximum allowable water pressure for the system while taking into account negative vacuum pressure on the outside of the sleeve. This was applied to all wetted surfaces and the inner O-ring surfaces to be conservative.

3.4. Results

Figure 7 shows the equivalent von-Mises stress and total deformation results. The maximum stress is located at the edge of the water port, where the hole of the inlet causes a 300% stress intensity of the approximately 6,600 kPa hoop stress in the cylinder [42]. The maximum stress of 19,870 kPa shown in Fig. 7(b) is well below the allowable stress of 75,150 kPa as listed in ASME BPVC Section II-D 2023 [41], yielding almost a safety factor of 4. The maximum deformation in the sleeve is seen near the O-ring groove in Fig. 7(c). However, it is minimal at 2.2×10^{-3} mm (83.5×10^{-7} in), and is not expected to cause enough deformation to compromise the seal.

C. Discussion

The temperature of the feedthrough body and internal ferrofluid are all kept within operating range by the addition of a cooling sleeve, though the bearing may need to be looked at more closely. The shaft itself reaches significantly high temperatures away from the feedthrough near the source of heating of the swing arm. As such, the shaft surface thermocouple should be monitored in real-time during long and high power runs to ensure it maintains sufficient strength to hold the model, which may require further analysis. Future cooling options that provide cooling to the swing arms themselves could be explored in order to decrease the shaft and swing arm temperature. The cooling water does not increase in temperature significantly so boiling is not a concern. Additionally, the fabricated sleeve does not see significant thermal stresses or pressure, and is well within the allowable stress given in the BPVC II for the material [41].

IV. Conclusions

In this project we formed a simple cooling sleeve design to protect the feedthrough component in our sweep arm assembly of the mARC II facility. This involved an analysis process that considered fluid dynamics, heat transfer, and mechanical stresses. Results show that at the highest predicted heating conditions, the cooling sleeve keeps the majority of the feedthrough within allowable operating temperatures. These results demonstrate that the cooling sleeve will greatly improve mARC II's capabilities by increasing sample dwell times, throughput, and reducing turnaround time between runs.

Future work will incorporate additional surface thermocouples along the sweep arm or shaft assembly. This will provide additional experimental data on the heating rate at different arc powers and nozzle distances. We also plan to re-design the sweep arm to allow for more than three samples in a single run, further increasing throughput.

Acknowledgments

Kathleen Edwards is supported through the NASA Amentum ATOM-5 contract No. 80ARC022DA011. Jocelino Rodrigues is the recipient of a NASA Postdoctoral Program (NPP) research fellowship at NASA Ames Research Center, administered by Oak Ridge Associated Universities (ORAU) under the NASA contract 80HQTR21CA005. The authors would like to thank Eric Noyes and Dr. Megan MacDonald for their inputs and support.

References

[1] Laub, B., "Use of Arc-Jet Facilities in the Design and Development of Thermal Protection Systems," *25th AIAA Aerodynamic Measurement Technology and Ground Testing Conference*, Vol. 1, American Institute of Aeronautics and Astronautics, 2006, pp. 514–527. DOI: 10.2514/6.2006-3292.

[2] Codron, D. A., and Nawaz, A., "Radial Profiles of Plasma Electron Characteristics in a 30 kW Arc Jet," *44th AIAA Plasmadynamics and Lasers Conference*, American Institute of Aeronautics and Astronautics, Reston, Virginia, 2013, pp. 1–12. DOI: 10.2514/6.2013-3128.

[3] Codron, D. A., Cruden, B. A., and Ho, T., "Emission Spectroscopy Characterization of Thermal Protection System Materials in Arc-Heated Flows," *45th AIAA Plasmadynamics and Lasers Conference*, American Institute of Aeronautics and Astronautics, Reston, Virginia, 2014, p. 2112. DOI: 10.2514/6.2014-2112.

[4] Miller, R. A., Tang, C. Y., McGlaughlin, M. S., White, T. R., Ho, T. S., MacDonald, M. E., and Cruden, B. A., "Characterization of a radiometer window for Mars aftbody heating including ablation product deposition using a miniature arc jet," *2018 Joint Thermophysics and Heat Transfer Conference*, American Institute of Aeronautics and Astronautics, Reston, Virginia, 2018, pp. 1–17. DOI: 10.2514/6.2018-3590.

[5] Luís, D., and MacDonald, M. E., "Emission spectroscopy characterization of electrode species in the freestream flow at the NASA Ames miniature Arc Jet II facility," *Journal of Quantitative Spectroscopy and Radiative Transfer*, Vol. 272, 2021, p. 107752. DOI: 10.1016/j.jqsrt.2021.107752.

[6] Haw, M. A., MacDonald, M. E., and Colom, S. V., "Big-data Efficient and Automated Science Transfer (BEAST): an open-source software architecture for arc jet data management, modeling, and automation," *AIAA SCITECH 2023 Forum*, American Institute of Aeronautics and Astronautics, Reston, Virginia, 2023, pp. 1–16. DOI: 10.2514/6.2023-2712.

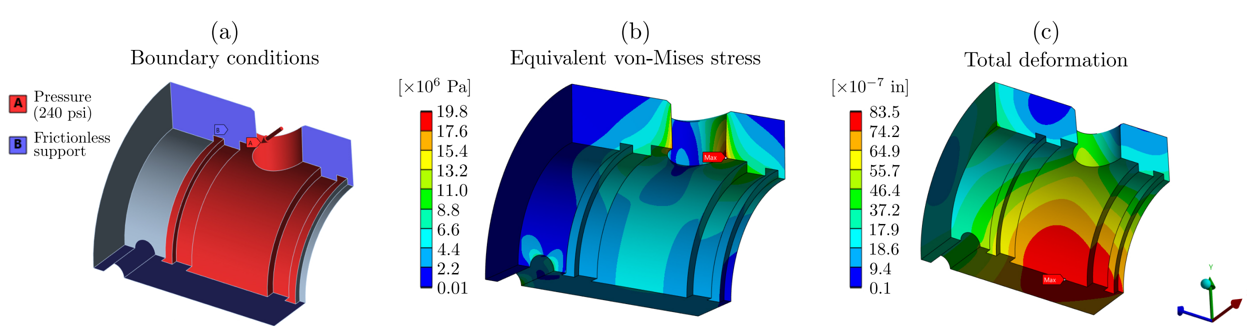

Fig. 7 Thermo-mechanical stress analysis: (a) boundary conditions; (b) von-Mises stress; (c) deformation.

[7] Rodrigues, J., Macdonald, M. E., Haw, M. A., Martinez, R., Philippidis, D., Colom, S., Chung, R., and Hartman, J., "Defining the Operational Envelope for Air Flows in the miniature Arc jet Research Chamber (mARC II)," *AIAA AVIATION FORUM AND ASCEND 2024*, AIAA, Las Vegas, Nevada, 2024. DOI: 10.2514/6.2024-3553.

[8] Colom, S. V., Haw, M. A., and Rodrigues, J., "Design and implementation of a fast-sweeping Langmuir probe diagnostic for DC arc jet environments," *Review of Scientific Instruments*, Vol. 96, No. 11, 2025. DOI: 10.1063/5.0272186.

[9] V. Colom, S., A. Haw, M., and Rodrigues, J., "First Characterization of RF Plasma Jet Using Spatially-Resolved OES and Fast-Sweeping Langmuir Diagnostics," *67th Annual Meeting of the APS Division of Plasma Physics (DPP)*, Long Beach, California, 2025. URL: https://archive.aps.org/dpp/2025/po06/4/.

[10] Rodrigues, J., "Thermochemically-Closed Sonic-Flow Inversion for Enthalpy and Temperature in Multispecies Arc-Jet Flows," *AIAA AVIATION 2026 FORUM*, American Institute of Aeronautics and Astronautics, San Diego, California, 2026.

[11] Rodrigues, J., "Closed-Form Reconstruction of Zoby–Sullivan Stagnation-Point Heat-Flux Scaling," *Journal of Thermophysics and Heat Transfer*, 2026.

[12] Rodrigues, J., MacDonald, M. E., Haw, M., Martinez, R., Philippidis, D., Colom, S., Chung, R. J., and Hartman, J., "Expanding the Measurement Capabilities of the mARC II Arc-Jet to Map the Operating Envelope for High-Enthalpy Air Flows," *AIAA SCITECH 2025 Forum*, American Institute of Aeronautics and Astronautics, Reston, Virginia, 2025. DOI: 10.2514/6.2025-2443.

[13] Palmer, G. E., Prabhu, D. K., Rodrigues, J., Driver, D. M., and Balboni, J. A., "CFD Simulations of Arcjet Experiments – A Survey of Recommended Practices and Lessons Learned," *AIAA AVIATION FORUM AND ASCEND 2025*, American Institute of Aeronautics and Astronautics, Reston, Virginia, 2025. DOI: 10.2514/6.2025-3480.

[14] Palmer, G. E., Prabhu, D., Driver, D. M., Rodrigues, J., and Balboni, J. A., "Computational Fluid Dynamics Simulations of Arcjet Experiments: Recommended Practices and Lessons Learned," *Journal of Thermophysics and Heat Transfer*, 2026, pp. 1–25. DOI: 10.2514/1.T7311.

[15] Terrazas-Salinas, I., "Test Planning Guide for NASA Ames Research Center Arc Jet Complex and Range Complex [A029-9701-XM3 Rev. J – July 28, 2022]," NASA Ames Research Center, 2022, URL: https://www.nasa.gov/wp-content/uploads/2023/07/tsf-test-planning-guide-revj.pdf.

[16] MacDonald, M., Rodrigues, J., Cushman, G., Martin, K., and Hartman, J., "Simultaneous Convective and Radiative Heating of Materials with the 200 kW Laser Enhanced Arc Jet Facility (LEAF)," *National Space & Missile Materials Symposium and Commercial and Government Responsive Access to Space Technology Exchange (NSMMS & CRASTE) Joint Symposia*, Tucson, AZ, 2023, pp. 1–18. URL: https://ntrs.nasa.gov/citations/20230008351.

[17] MacDonald, M. E., Philippidis, D., Haw, M., Schickele, D., Luis, D., Hartman, J., and McGlaughlin, M., "Initial Characterization of the 30 kW Miniature Arc Jet (mARC II) at NASA Ames Research Center," *AIAA AVIATION 2020 FORUM*, American Institute of Aeronautics and Astronautics, Reston, Virginia, 2020, pp. 1–15. DOI: 10.2514/6.2020-3108.

[18] MacDonald, M. E., Haw, M. A., Martinez, R., Colom, S., Rodrigues, J., Chung, R., and Hartman, J., "Characterizing Heat Flux in the miniature Arc jet Research Chamber (mARC II)," *AIAA AVIATION 2023 Forum*, American Institute of Aeronautics and Astronautics, San Diego, California, 2023, pp. 1–9. DOI: 10.2514/6.2023-3298.

[19] Marshall, P., Caldwell, A., Feldman, J., Chavez-Garcia, J., Hendrickson, K., Rodrigues, J., MacDonald, M., Turcotte, A., Alcantara, T., Swaiss, C., and Bebak, A., "Designing Insulative Reusable Thermal Protection Materials – from Shuttle Tile to Next Generation Systems," *Composites, Materials, & Structures (CMS 2025) 48th Annual Conference*, 2025.

[20] Vallone, E., Agnello, G., Basili, L., Ciampichetti, A., Di Maio, P., Lioce, D., Quartararo, A., and Venturi, F., "Thermal-hydraulic assessment of the ITER IBED PHTS," *Fusion Engineering and Design*, Vol. 203, 2024, p. 114449. DOI: 10.1016/j.fusengdes.2024.114449.

[21] Agnello, G., Ciampichetti, A., Dell'Orco, G., Maio, P. A. D., Palma, G. D., Farinella, F. M., Maggio, S., and Vallone, E., "Thermal-hydraulic analysis of the ITER CCWS-1 cooling loop," *Fusion Engineering and Design*, Vol. 211, 2025, p. 114766. DOI: 10.1016/j.fusengdes.2024.114766.

[22] Sessler, J. G., and Weiss, V., *Aerospace Structural Metals Handbook: Volume 1. Ferrous Alloys*, Air Force Materials Laboratory, Air Force Systems Command, United States Air Force, 1967. URL: https://ntrl.ntis.gov/NTRL/dashboard/searchResults/titleDetail/AD737970.xhtml.

[23] Ferrotec Corporation, "APGO series / APGOn series magnetic fluid (Chemical Safety Data Sheet)," , 2017, URL: https://ferrofluid.ferrotec.com/wp-content/uploads/sites/3/apgOsds.pdf.

[24] Ferrotec Corporation, "APG O27N Specifications and Physical Properties," , 2026. URL: https://ferrofluid.ferrotec.com/products/ferrofluid-audio/apg-o/apg-o27n/.

[25] Bruno, T. J., Fortin, T. J., Huber, M. L., Laesecke, A., Lemmon, E. W., Mansfield, E., McLinden, M. O., Outcalt, S. L., Perkins, R. A., Urness, K. N., and Widegren, J. A., "Thermophysical properties of polyol ester lubricants," National Institute of Standards and Technology, Gaithersburg, MD, 8 2019, DOI: 10.6028/NIST.IR.8263.

[26] "Computational and Experimental Assessment of Jets in Cross Flow," Advisory Group for Aerospace Research & Development (AGARD), Neuilly Sur Seine, France, 1993, URL: https://apps.dtic.mil/sti/tr/pdf/ADA275733.pdf.

[27] SMITH, S. H., and MUNGAL, M. G., "Mixing, structure and scaling of the jet in crossflow," *Journal of Fluid Mechanics*, Vol. 357, 1998, pp. 83–122. DOI: 10.1017/S0022112097007891.

[28] Dean, W., "XVI. Note on the motion of fluid in a curved pipe," *The London, Edinburgh, and Dublin Philosophical Magazine and Journal of Science*, Vol. 4, No. 20, 1927, pp. 208–223. DOI: 10.1080/14786440708564324.

[29] Menter, F. R., "Improved two-equation k-omega turbulence models for aerodynamic flows [TM 103975]," NASA, 1992, URL: https://ntrs.nasa.gov/citations/19930013620.

[30] Menter, F. R., "Zonal two equation κ-ω turbulence models for aerodynamic flows," *AIAA 23rd Fluid Dynamics, Plasmadynamics, and Lasers Conference, 1993*, American Institute of Aeronautics and Astronautics Inc, AIAA, 1993. DOI: 10.2514/6.1993-2906.

[31] Menter, F. R., "Two-equation eddy-viscosity turbulence models for engineering applications," *AIAA Journal*, Vol. 32, No. 8, 1994, pp. 1598–1605. DOI: 10.2514/3.12149.

[32] Hellsten, A., "Some improvements in Menter's k-omega SST turbulence model," *29th AIAA, Fluid Dynamics Conference*, American Institute of Aeronautics and Astronautics, Reston, Virigina, 1998, pp. 1–11. DOI: 10.2514/6.1998-2554.

[33] Menter, F. R., Kuntz, M., and Langtry, R., "Ten Years of Industrial Experience with the SST Turbulence Model," *Turbulence, Heat and Mass Transfer*, Vol. 4, 2003, pp. 625–632. URL: https://www.researchgate.net/profile/Florian-Menter/publication/228742295_Ten_years_of_industrial_experience_with_the_SST_turbulence_model/links/0046353c6330b1c0a4000000/Ten-years-of-industrial-experience-with-the-SST-turbulence-model.pdf.

[34] Menter, F. R., "Review of the shear-stress transport turbulence model experience from an industrial perspective," *International Journal of Computational Fluid Dynamics*, Vol. 23, No. 4, 2009, pp. 305–316. DOI: 10.1080/10618560902773387.

[35] Kays, W. M., "Turbulent Prandtl Number—Where Are We?" *Journal of Heat Transfer*, Vol. 116, No. 2, 1994, pp. 284–295. DOI: 10.1115/1.2911398.

[36] Rhie, C. M., and Chow, W. L., "Numerical study of the turbulent flow past an airfoil with trailing edge separation," *AIAA Journal*, Vol. 21, No. 11, 1983, pp. 1525–1532. DOI: 10.2514/3.8284.

[37] Paul G. Tucker, *Advanced Computational Fluid and Aerodynamics*, Cambridge University Press, 2015. DOI: https://doi.org/10.1017/CBO9781139872010.

[38] Knoll, D., and Keyes, D., "Jacobian-free Newton–Krylov methods: a survey of approaches and applications," *Journal of Computational Physics*, Vol. 193, No. 2, 2004, pp. 357–397. DOI: 10.1016/j.jcp.2003.08.010.

[39] Kelley, C. T., and Keyes, D. E., "Convergence Analysis of Pseudo-Transient Continuation [ICASE Report No. 96-46]," , 1996, URL: https://apps.dtic.mil/sti/tr/pdf/ADA314613.pdf.

[40] Patankar, S. V., *Numerical Heat Transfer and Fluid Flow*, 1st ed., CRC Press, 1980. DOI: https://doi.org/10.1201/9781482234213.

[41] ASME's Boiler and Pressure Vessel Code (BPVC), "BPVC-II-D, Section. II, Part D, Properties, Customary or Metric," ASME, 2023, URL: https://www.asme.org/getmedia/1d2fce12-9ebd-46c0-bec6-64ebfcc3f1d3/bpvc_form_2023.pdf.

[42] Pilkey, W. D., and Pilkey, D. F., *Peterson's Stress Concentration Factors*, Wiley, 2007. DOI: 10.1002/9780470211106.